The Ecology of Dense Star Clusters with Binaries

Simon F. Portegies Zwart[1]

Astronomical Institute 'Anton Pannekoek' and Section Computational Science, University of Amsterdam, Kruislaan 403, 1098SJ Amsterdam, the Netherlands
spz@science.uva.nl

Summary. We study the first 100 Myr of the evolution of isolated star clusters with 117965 single stars and 13107 primordial hard binaries. Our calculations include stellar and binary evolution. The early evolution of these clusters can be characterized by three distinct phases, which we dubbed **A**, **B** and **C**. Here phase **A** lasts for the first ~ 3 Myr and is dominated by two-body relaxation, phase **B** lasts to about 20–100 Myr and is dominated by stellar mass loss, after that phase **C** sets in, which again is dominated by two-body relaxation. The presence of the primordial binaries has little effect on these various stages, nor on the other conclusions we draw here. The mass function of the main-sequence stars in the core becomes as flat as $x = -1.8$ (initial Salpter was $x = -2.35$), and in the outer 10% (by mass) of the cluster the mass function exponent is as steep as $x = -2.6$. Over the lifetime of the star cluster, a large number of stellar-mass black holes and neutron stars are formed. Roughly 50%–70% of the black holes are retained by the clusters, whereas the neutron star retention fraction is about 7%–12%. A relatively large fraction of black holes become members of a binary either with another black hole ($\sim 40\%$) or with another stellar companion ($\sim 50\%$). We conclude that in young (but $\gtrsim 50$ Myr) star clusters the X-ray binaries with a black hole may outnumber those with a neutron star by about a factor of 3.

1 Introduction

The early evolution of dense clusters of stars is of considerable interest, in part to develop a better understanding of the conditions under which star clusters are born, and in part to be able to identify the dynamical state of observable star clusters. The initial conditions of star clusters have been debated actively over the years, but no consensus has been reached either by studying or simulating the formation process of stellar conglomerates or from simulating or observing older systems. The main parameters which characterize a star cluster at birth (and any time later) are the richness, mass function, stellar velocity distribution, etc, all as a function of the three space coordinates.

Part of the problem comes from our static view of the universe, our inability to run simulations backward with time and our lack of understanding of the physics of the star(cluster) formation process. In this paper we take the approach of starting with a pre-selected set of initial conditions, based on observations, and compute the evolution of the star cluster.

2 Simulations

In this study we simulate young, $\leq 100\,\mathrm{Myr}$, star clusters by integrating the equations of motion of all stars and binaries. We use the Starlab environment [15], which acquires it's greatest speed on the GRAPE-6 special purpose computer (GRAvity PipE, [10, 9]). We use the hardware at the university of Tokyo, the MoDeStA[1] platform in Amsterdam and the GRAPE-6 setup at Drexel university for the calculations presented here.

The simulated star clusters are initialized by selecting the number of stars, stellar mass function, binary fraction and their orbital elements and the density profile. For our most concentrated model (simulation #1) we adopt the initial conditions derived by Portegies Zwart et al. [14] to mimic the 7-12 Myr old star cluster MGG-11 in the star-burst galaxy M82, which was observed in detail by McCrady et al [11]. In this paper, however, we extend the evolution of this model to about 100 Myr. Subsequent simulations are performed with larger cluster radius, resulting in longer initial relaxation times. The stellar evolution model adopted is based on [1], and the binaries are evolved with SeBa [16].

We summarize the selection of the initial conditions for simulation #1: first we selected 131072 stars distributed in a King [6] density profile with $W_0 = 12$ and with masses from a Salpeter initial mass function ($x = -2.35$) between $1\,M_\odot$ and $100\,M_\odot$. The total mass of the cluster is then $M \simeq 433000\,M_\odot$. The location in the cluster where the stars are born is not correlated with the stellar mass, i.e. there is no primordial mass segregation. Ten percent of the stars were randomly selected and provided with a companion (secondary) star with a mass between $1\,M_\odot$ and the mass of the selected (primary) star from a flat distribution. The binary parameters were selected as follows: first we chose a random binding energy between $E = 10\,\mathrm{kT}$ (corresponding to a maximum separation of about $1000\,R_\odot$). The maximum binding energy was selected such that the distance at pericenter exceeded four times the radius of the primary star. At the same time we select an orbital eccentricity from the thermal distribution. If the distance between the stars at pericenter is smaller than the sum of the stellar radii we select a new semi-major axis and eccentricity. If necessary, we repeat this step until the binary remains detached. As a result, binaries with short orbital periods are generally less eccentric. We ignored an external tidal field of the Galaxy, but stars are removed from the simulation if they are more than 60 initial half-mass radii away from the density center of the cluster.

For the other simulations #2, #3 and #4, we adopt the same realization of the initial stellar masses, position and velocities (in virial N-body units [5]) but with a different size and time scaling to the stellar evolution, such that the two-body relaxation time ($t_{\rm rh}$) for simulation #2 is four times that of #1, for simulation #3 we used four times the two-body relaxation time of what was

[1] see `http://modesta.science.uva.nl`

used for simulation #2, etc. the initial conditions are summarized in Tab. 1. The binary populations in the various initial realizations therefore have larger maxima to the orbital separation in the clusters with a longer relaxation time, because the adopted maximum binding energy of 10 kT shifts. For the simulations #2, #3 and #4, the maximum orbital separations are about $2000\,R_\odot$, $5000\,R_\odot$ and $10^4\,R_\odot$, respectively.

Table 1. Conditions for the four runs performed with 144179 stars (including 10% primordial hard binaries) with a range of cluster radii. Density profiles are taken from King with $W_0 = 12$. The columns give the model name, the initial virial radius and core radius followed by the initial crossing time and half-mass relaxation time. The last column indicates the moment when core collapse happened in these simulations.

Run	$r_{\rm vir}$, pc	$r_{\rm core}$, pc	$t_{\rm ch}$, Myr	$t_{\rm rh}$, Myr	$t_{\rm cc}$ Myr
#1	1.27	0.010	0.032	80	40
#2	3.2	0.026	0.129	320	77
#3	8.1	0.066	0.516	1300	$\gtrsim 100$
#4	20	0.162	2.067	5100	$\gtrsim 100$

After initialization we synchronously calculate the evolution of the stars and binaries, and solve the equations of motion for the stars in the cluster. The calculations are continued to an age of about 100 Myr.

During the integration of simulation #2, the energy is conserved on average better than one part in $10^{7.1\pm1.7}$ per crossing time, with a total of $\sim 10^{-4}$ difference between the final and initial energy. For the other runs the energy is conserved at least an order of magnitude better.

Following the paper *Star Cluster Ecology VI* by Portegies Zwart, McMillan & Makino (in preparation, see also [13]), we divide the evolution of star clusters into four distinct phases, each of which is characterized by rather typical parameters. We call them phase **A**, **B**, **C** and phase **Z**. The four phases are classified as follows: phase **A** is an early relaxation dominated phase, followed by phase **B** in which the $\sim 1\%$ (by number) of the most massive stars quickly evolve and lose an appreciable fraction of their mass. Finally, phase **C** starts when stellar evolution slows down and two-body relaxation becomes dominant again. To complete this classification we introduce phase **Z** in which the cluster dissolves due to tidal stripping, but we will not discuss this phase in detail (see [7] for a more analytical approach to phase **Z**).

In Fig. 1 we present the evolution of the core radius, the 5%, 25%, 50% and 75% Lagrangian radii for simulation #2. The three phases of cluster evolution **A**, **B**, and **C** are indicated by the horizontal bar near the bottom of the figure. In phase **A** the cluster expands slowly followed by a more rapid expansion in phase **B**. This latter phase is mainly driven by stellar mass loss. During phase **C** the cluster re-collapses as relaxation processes start to dominate again over stellar mass loss. This leads to a collapse of the cluster core at an age of about 80 Myr.

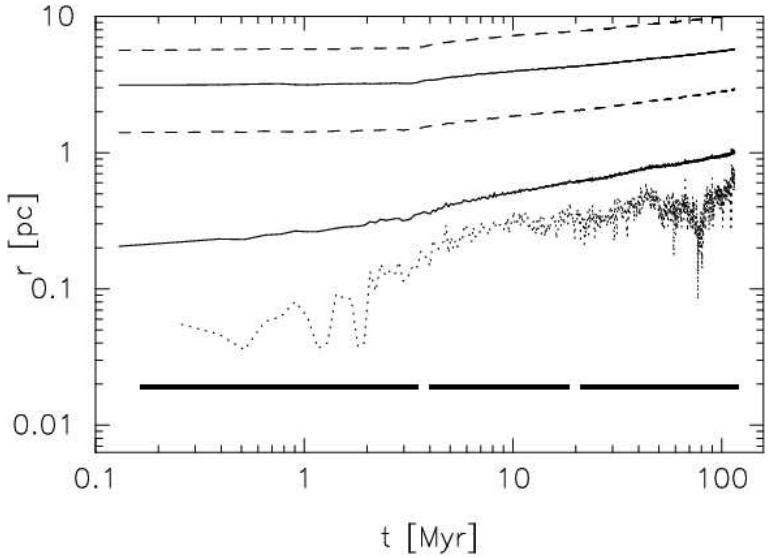

Fig. 1. Evolution of the core radius (dotted curve), 5% Lagrangian radius (lower solid), 25% (lower dashed line), half mass radius (upper solid) and 75% Lagrangian (upper dashed line) radii for the simulation #2. The areas for evolutionary phases **A**, **B**, and **C** are indicated with the three horizontal bars near the bottom of the plot.

3 Evolution of the Binding Energies

A seizable fraction of the total potential energy of the simulated star clusters is locked-up in primordial binaries. This energy can be released by dynamical encounters and by stellar evolution.

In Fig. 2 we present the evolution of the energy for simulation #3. The lower dashed line gives the total binding energy in the binaries in dimensionless N-body units [5]. Throughout the evolution of the cluster, this number remains smaller than the total potential energy (lower solid curve in Fig. 2).

The kinetic energy in simulation #3 in the early part ($\lesssim 50\,\mathrm{Myr}$) is governed by supernova remnants (neutron stars and black holes) which tend to receive high velocity kicks upon formation. Once these objects have escaped the cluster the curve flattens out. It is interesting to note that the cluster is, technically speaking, unbound in this early phase, but it remains bound as most of this energy escapes the cluster without heating it effectively. Strictly speaking, this is a bookkeeping problem in the simulation, as one could wonder if a high-velocity neutron star should be counted as a member while it is still within the cluster perimeter but with a velocity exceeding the escape speed.

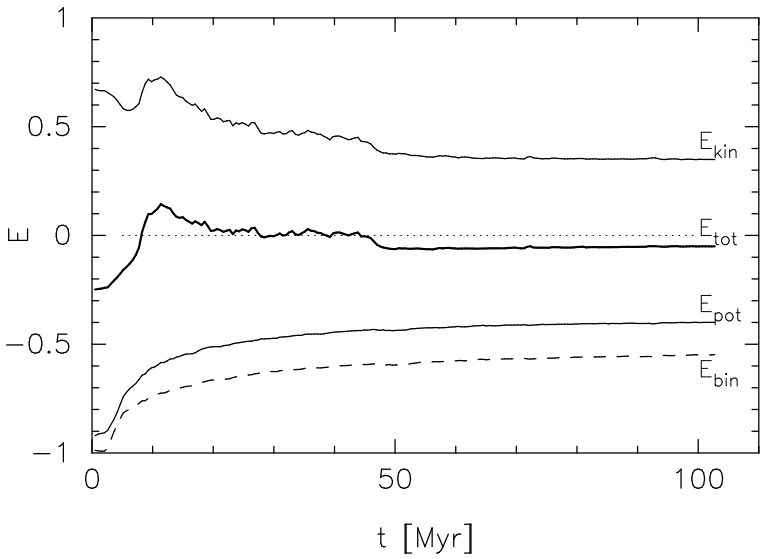

Fig. 2. Evolution of the kinetic, potential and total energy for the simulation #3. The dashed line gives the evolution of the binding energy of the binary population, which was subtracted from the potential and total energies. The dotted line, drawn to guide the eye, indicates regions where the total kinetic energy of the cluster exceeds the potential energy.

3.1 Evolution of the Mass Function

All simulations started with a Salpeter ($x = -2.35$) mass function. In due time the mass function changes – in part globally due to stellar evolution and selective evaporation, which is initiated by the dynamical evolution of the cluster. With time, the mass function also starts to vary locally due to mass segregation. It is hard to disentangle all effects and identify the relative importance of each. To qualify and quantify the changes to the global

and local mass function we first select those stars which remain on the main sequence during the studied cluster evolution. The turn-off mass at 100 Myr in our stellar evolution model is about $4.63\,M_\odot$ and stars exceeding a mass of $5.54\,M_\odot$ have all turned into remnants. By limiting ourselves to main-sequence stars in this rather small mass range we guarantee that the mass function is not polluted by blue stragglers, giants or stellar remnants. Therefore we measure the mass function exponent for main-sequence stars between $1\,M_\odot$ and $4.5\,M_\odot$.

Throughout the evolution of our clusters, and irrespective of the cluster location, the mass function between $1\,M_\odot$ and $4.5\,M_\odot$ remains accurately represented by a power-law, which is another important motivation to adopt this seemingly arbitrary mass range.

In Fig. 3 we present the evolution of the slope of the cluster mass function between $1\,M_\odot$ and $4.5\,M_\odot$ for simulation #1. The exponent was calculated with a least-squares fit to the binned (100 bins) mass function in the appropriate range. The global mass function is fitted with a power-law to better than in 2%, for the 10% Lagrangian radii the fit is always better than 6%, consistent with the expected variation from the Poissonian noise. The various curves represent the mass function within (or outside) the 50%, 25% and 10% Lagrangian radii, for the dashed, dotted and dash-3-dotted curves respectively.

The global mass function (solid curve) in the adopted mass range becomes slightly steeper with time, from $x \simeq -2.41$ at birth to about $x \simeq -2.43$ at an age of 100 Myr, for the simulation #1. The rate of change of the mass function exponent is $\dot{x} \simeq -2.7 \times 10^{-4}$ per Myr, and constant with time after 60 Myr. Similar trends in the global mass function are observed in the other models, though in these cases the changes in x are less regular and more noisy, therefore we decided to show the results for the simulation #1.

The steepening of the main-sequence mass function can be explained by dynamical activity in the cluster center, where relatively high-mass stars tend to be ejected from the cluster more frequently than lower-mass stars. It happens because the latter are not as abundant in the cluster core, and lower-mass stars are less frequently participating in strong dynamical encounters. The change of the global mass function is then mainly driven by strong dynamical encounters in the cluster core and not per se by selective evaporation near the tidal radius. The change in behavior around 60 Myr is caused by the formation of white dwarfs, which tend to compete with the $\sim 1\,M_\odot$ main-sequence stars. Neutron stars are not participating in this competition as the majority of these escape due to the high velocities they receive upon birth.

The mass functions for the outer 10%, 25% and 50% Lagrangian radii become steeper with time, with an exponent of $x \simeq -2.56$ for the outer 50% to $x \simeq -2.64$ for the outer 10% Lagrangian radius in simulation #1. The mass function in the inner parts of the cluster becomes flatter with time.

Within the half-mass radius the mass function flattens to $x \simeq -2.3$ in about 100 Myr and for the inner 10% Lagrangian radius the mass function flattens to $x \simeq -1.9$.

The change in the mass function in the inner part of the cluster can be described with

$$x(t) = x(0) + \left(\frac{t}{\tau}\right)^{0.5}. \quad (1)$$

Here $x(0)$ in the initial power-law slope, and τ is a constant. For the inner 10% Lagrangian radius $\tau \sim 400$ Myr; $\tau \sim 1.2$ Gyr; for the inner 25% Lagrangian radius and $\tau \sim 10$ Gyr for the mass function within the half-mass radius. This expression is presented in Fig. 3 as the upper solid curve fitting the mass function in the inner 10% Lagrangian radius.

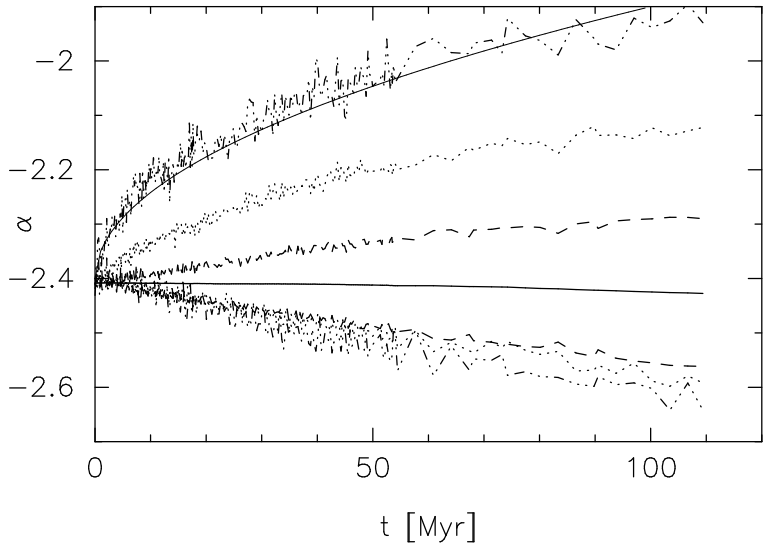

Fig. 3. Evolution of the power-law slope of the mass function of main-sequence stars between $1\,M_\odot$ and $4.5\,M_\odot$ for the run #1. The solid (almost) horizontal curve represents the entire cluster, the curves above (flatter mass function) are for the inner part of the cluster, the lower curves (steeper mass function) are for the outer parts outside the adopted Lagrangian radius. The dashed, dotted and dash-3-dotted curves give the mass function exponent for the stars withing (respectively, outside) the 50%, 25% and 10% Lagrangian radii. The thin solid line through the upper dash-3-dotted curve (mass function within the 10% Lagrangian radius) is calculated with $x \propto \sqrt{t}$ (see text). Note that after 55 Myr we increased the time interval between snapshot outputs from 1 Myr to 5 Myr.

3.2 Black Hole and Neutron Star Retention

In Fig. 4 we present the stellar content of the simulation #2 for the entire cluster (solid curves) and inside the inner 10% Lagrangian radius (dotted curves). The fraction of main-sequence stars (below the lower solid curve) and binaries (above the top solid curve) gradually decrease with time, whereas the fraction of giants (between the lower and middle solid curve) and stellar remnants (between the middle and top solid curve) increases with time. The figure clarifies that at later age contribution of giants and stellar remnants is considerable, and that in particular the number of compact remnants continue to grow quite rapidly after about 50 Myr. This change in behavior, around 50 Myr, is mainly caused by the formation of white dwarfs, which quickly start to dominate the population of stellar remnants, whereas the fraction of evolved stars (giants) remains roughly constant. Note also that the binary fraction decreases slightly with time.

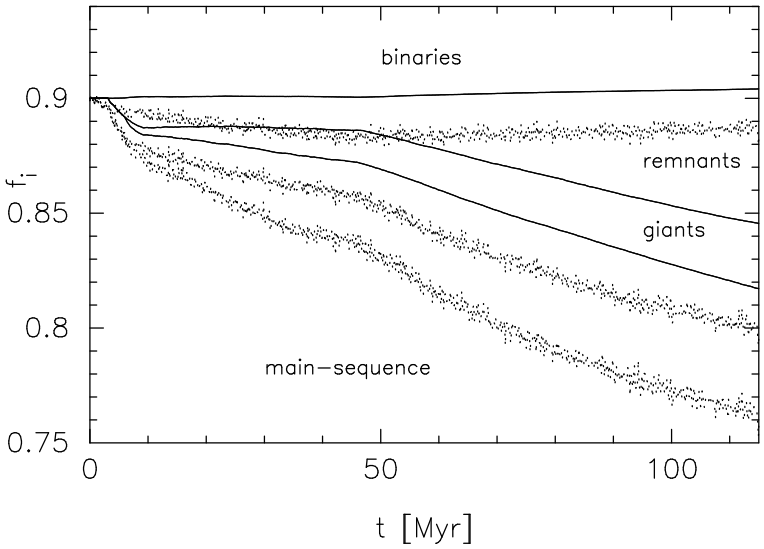

Fig. 4. The stellar content of the simulation #2 as a function of time, for the entire cluster (solid curves) and for the inner 10% Lagrangian radius (dotted curves). The lower lines give the fractional contents of main-sequence stars, followed by the evolved stars (giants) and compact objects (remnants). The top area indicates that the binary fraction reduces only slightly from it initial value of 0.1 throughout the simulation. All fractions add-up to 1.

In our simulations, black holes and neutron stars receive kicks upon formation. Neutron star kicks are selected from the Paczynski velocity distribution with a dispersion of $\sigma_{\rm kick} = 300\,{\rm km\ s^{-1}}$ [4], whereas a black hole of mass

$m_{\rm bh}$ receives a kick from the same distribution but smaller by a factor of $1.4\,M_\odot/m_{\rm bh}$.

In each run about 1700 black holes were formed in type Ic supernovae, and 6500 neutron stars were formed in type Ib and type II supernovae. Though the initial realizations for the various runs were identical the numbers of supernovae differ slightly from run to run, with more supernovae occurring in the larger (lower-density) clusters. This is mainly caused by selective evaporation of massive stars and by variations in binary evolution. Massive stars are preferentially ejected in strong dynamical encounters, which are more common in the denser clusters. These clusters are also more prone to binary evolution, as the orbital periods are on average shorter.

The retention fraction for black holes varies between 0.48 and 0.71, for neutron stars this fraction is between 0.065 and 0.12. The difference between the lowest and highest retention fractions is about a factor of two. In both cases, more compact objects are retained in the denser clusters. This is a direct consequence of the larger escape speed of the denser clusters, through which fewer black holes and neutron star are able to escape.

A seizable fraction of the compact objects remain in binaries. While initially 10% of the stars were binary members, about 4% of the compact objects are ultimately binary members, which is a rather large fraction considering relatively small ($\lesssim 10\%$) retention fraction.

The majority of the binaries consisting of a compact object with a stellar companion (indicated by $\star$ in Table 2) will turn into X-ray binaries at some moment in time. Such binaries with a black hole outnumber those with a neutron star by about a factor of 2 to 4. Based on these numbers, we conclude that in star clusters which are old enough to have produced most of their black holes and neutron stars, the population of X-ray binaries with a black hole outnumbers those with a neutron star by a factor of 2–4. Such clusters would then be very interesting objects for further X-ray studies. Note, however, that the choice of a lower limit of $1\,M_\odot$ for the initial mass function tends to boost the number of black holes and neutron stars, and the production of black-hole X-ray binaries will be less efficient in star clusters with a lower cut-off to the mass function.

Even though binary black holes are quite common in our simulations, they generally have rather wide orbits. This has the interesting consequences that these binaries will experience Roche-lobe overflow when the stellar companion is a giant, resulting in a rather short but bright X-ray phase. On the other hand, these binaries are not candidates for ground-based gravitational wave detectors. Binaries with two neutron stars have difficulty to survive; none were formed in any of our simulations.

In Fig. 5 we present the number of binaries with at least one compact object (black hole, neutron star or white dwarf) as a function of time. The number of black holes in binaries rises sharply shortly after the start of the simulation with a peak near 8 Myr. This is the moment when the turn-off

Table 2. Some characteristics of the compact objects at 100 Myr (see text).

Run	$N_{\rm Ic}$	$N_{\rm Ib+II}$	$N_{\rm bh}$	$N_{\rm ns}$	(bh,bh)	(bh,ns)	(ns,ns)	(bh,$\star$)	(ns,$\star$)
#1	1656	6584	1017	585	12	1	0	15	6
#2	1710	6446	1028	553	16	4	0	21	6
#3	1717	6387	834	365	17	2	0	20	3
#4	1728	6735	828	436	11	4	0	16	10

drops below the minimum mass for forming black holes (at $\sim 20\,M_\odot$), and lower-mass stars form neutron stars. This is also visible in the sharp increase of the number of binaries with a neutron star. The number of black holes in binaries drops rapidly from this moment because many of their companions form neutron stars in a supernova explosion. These newly formed neutron stars receive a much higher asymmetric kick velocity during their formation [8] than black holes [3]. Note here that binary containing a neutron star and a black hole are counted twice, once among the (bh,$\star$) and once for (ns,$\star$).

The solid curves in the bottom panel of Fig. 5 show an interesting depression between about 75 Myr and 80 Myr. It appears that the binaries with a white dwarf located within $2\,r_{\rm core}$ become depleted. This is not really the case, but rather the cluster experiences a phase of core collapse. This may not be so surprising at first, if one imagines that core collapse tend to happen in about 15%–20% of the half-mass relaxation time [12]. For this cluster, the half-mass relaxation time is about 440 Myr and the core collapse is therefore expected at an age of about 65–85 Myr, which is consistent with the moment of core collapse in simulations without primordial binaries.

The moment of core collapse is therefore unaffected by the relatively rich population of hard primordial binaries in these simulations. We conclude that the primordial binary fraction and their distribution in hardness is relatively unimportant for the moment of core collapse. This result is contradicted by other Monte-Carlo simulations which tend to indicate that core collapse is strongly delayed by the presence of a rich binary fraction [2].

White dwarfs start to dominate the population of compact binaries after about 25 Myr, at a turn-off mass of about $10\,M_\odot$. Stars of $\lesssim 8\,M_\odot$ which evolve in isolation, unperturbed from a companion star, turn into white dwarfs, but in a binary system early stripping of the hydrogen envelope may cause a more massive star to become a white dwarf instead of collapsing to a neutron star. The population of compact binaries in clusters older than about 40 Myr is dominated by white dwarfs. But it may take a long while before they also become more common than the primordial main-sequence binaries.

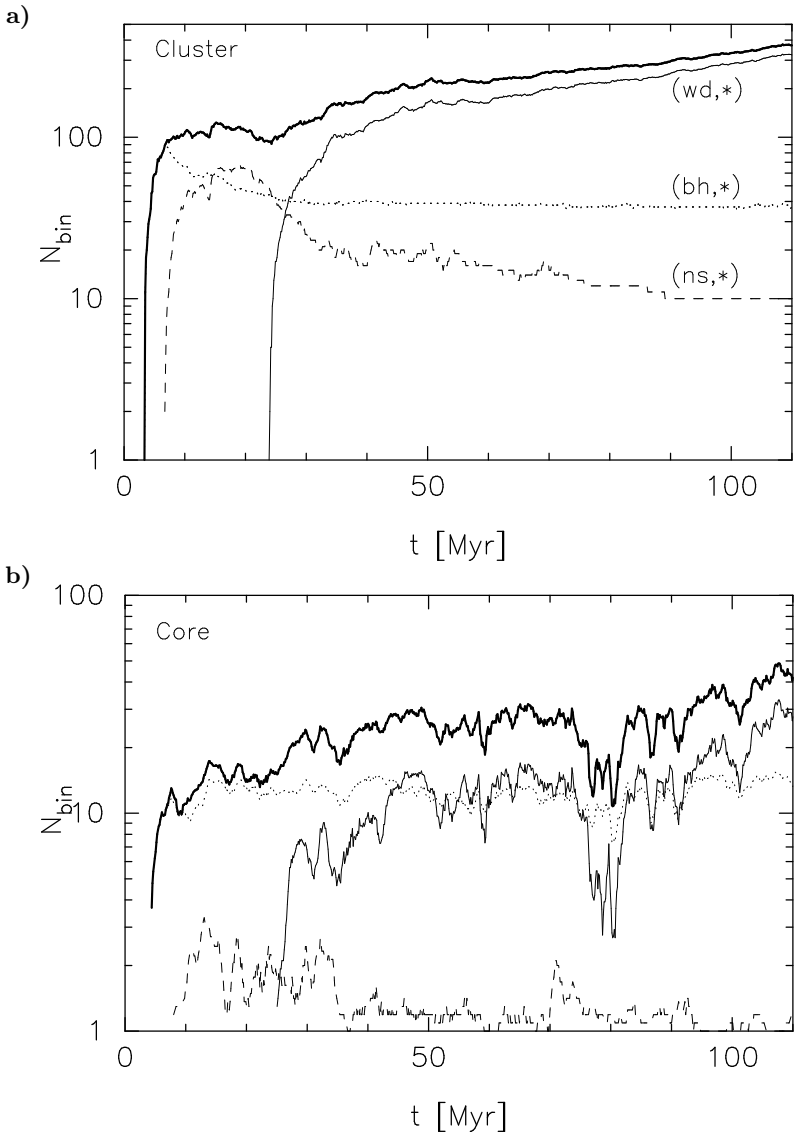

Fig. 5. The number of binaries with a compact object as a function of time for run #2. The top panel (a) gives numbers for the entire cluster, and the bottom panel (b) – within $2r_{\rm core}$. The top (thick solid) curve gives the total number of binaries with at least one compact object (bh, ns or wd). The thin solid curve gives the number of binaries with one white dwarf, the dashed curve is for neutron stars and the dotted curve for binaries with at least one black hole. Note that binaries with two compact objects are counted twice in this statistics and, as a consequence, the total of thin curves does not add-up to the thick curve.

Acknowledgments

I am grateful to Steve McMillan, Jun Makino, Piet Hut and Holger Baumgardt for numerous discussions. I am also grateful to Tokyo University for the use of their GRAPE-6 hardware. This work was supported by NWO (via grant #630.000.001), NOVA, the KNAW and the LKBF. The MoDeStA computer in Amsterdam was used extensively for this work.

References

1. P.P. Eggleton, M.J. Fitchett, C.A. Tout: ApJ, **347**, 998 (1989)
2. J. M. Fregeau, M.A. Gürkan, K.J. Joshi, & F. Rasio, ApJ, **593**, 772 (2003)
3. A. Gualandris, M. Colpi, S.F. Portegies Zwart, & A. Possenti, ApJ, **618**, 845 (2005)
4. J.W. Hartman, A&A **322**, 127 (1997)
5. D.C. Heggie, R. Mathieu: in: P. Hut, S. McMillan (eds.), Lecture Not. Phys. **267**, Springer-Verlag, Berlin (1986)
6. I.R. King: AJ, **71**, 64 (1966)
7. H.J.G.L.M. Lamers, M. Gieles, S.F. Portegies Zwart: A&A, **429**, 173 (2005)
8. A. G. Lyne, & D.R. Lorimer, Nature, **369**, 127 (1994)
9. J. Makino, T. Fukushige, M. Koga, K. Namura: PASJ, **55**, 1163 (2003)
10. J. Makino, M. Taiji, T. Ebisuzaki, D. Sugimoto: ApJ, **480**, 432 (1997)
11. N. McCrady, A.M. Gilbert, J.R. Graham: ApJ, **596**, 240 (2003)
12. S.L.W. McMillan, & S.F. Portegies Zwart, ApJ, **596**, 314 (2003)
13. S.F. Portegies Zwart: Book of the Como School of Physics, *Joint Evolution of Black Holes and Galaxies*, Graduate School in Contemporary Relativity and Gravitational Physics (2004)
14. S.F. Portegies Zwart, H. Baumgardt, P. Hut, J. Makino, S.L.W. McMillan: Nature, **428**, 724 (2004)
15. S.F. Portegies Zwart, S.L.W. McMillan, P. Hut, J. Makino: MNRAS, **321**, 199 (2001)
16. S.F. Portegies Zwart, F. Verbunt: A&A, **309**, 179 (1996)